Bull Volcanol (1998) 60:239–251

ORIGINAL PAPER

M. E. MacKay · S. K. Rowland
P. J. Mouginis-Mark · H. Garbeil

Thick lava flows of Karisimbi Volcano, Rwanda: insights from SIR-C interferometric topography

Received: 6 September 1997 / Accepted: 15 May 1998

Abstract We use a digital elevation model (DEM) derived from interferometrically processed SIR-C radar data to estimate the thickness of massive trachyte lava flows on the east flank of Karisimbi Volcano, Rwanda. The flows are as long as 12 km and average 40–60 m (up to >140 m) in thickness. By calculating and subtracting a reference surface from the DEM, we derived a map of flow thickness, which we used to calculate the volume (up to 1 km^3 for an individual flow, and 1.8 km^3 for all the identified flows) and yield strength of several flows (23–124 kPa). Using the DEM we estimated apparent viscosity based on the spacing of large folds (1.2×10^{12} to 5.5×10^{12} Pa s for surface viscosity, and 7.5×10^{10} to 5.2×10^{11} Pa s for interior viscosity, for a strain interval of 24 h). We use shaded-relief images of the DEM to map basic flow structures such as channels, shear zones, and surface folds, as well as flow boundaries. The flow thickness map also proves invaluable in mapping flows where flow boundaries are indistinct and poorly expressed in the radar backscatter and shaded-relief images.

Key words Karisimbi · Virunga · Viscous lava flows · Lava rheology · Remote sensing

Introduction

Field studies of Karisimbi Volcano (Fig. 1) have mapped flow boundaries, collected samples for petrologic study, and dated individual flows (DeMulder 1981, 1985; DeMulder and Pasteels 1986; Marcelot et al. 1985). From these studies, DeMulder (1985) has drawn a morphologic and structural evolution of Karisimbi that culminates in the eruption of viscous lava flows and domes on the east flank. These late-stage effusions range from flows that are more than 140 m thick but extend no more than a few kilometers from the vent, to 12-km-long flows that average 40–60 m in thickness and possess well-defined channels and arcuate ridges. The gross morphology of the Karisimbi flows can be seen in the contour map of Thonnard et al. (1965); however, many areas of the volcano remain poorly explored owing to difficult and inaccessible terrain.

In this study we present topographic analyses of Karisimbi Volcano using a detailed new digital elevation model (DEM) that we derived from SIR-C data using radar interferometry (Zebker and Goldstein 1986; Massonet and Rabaute 1993; Zebker et al. 1994). We use this DEM to make shaded-relief images, from which we map topographic features, and to create a flow-thickness map. From flow thickness and area we calculate volume. Using previously derived relationships for rheological parameters, we estimate yield strength of individual flows from cross-flow profiles and apparent viscosity from the height and spacing of surface folds. These topographic analyses add a heretofore missing aspect to our understanding of Karisimbi Volcano and another data set to the morphologic studies of viscous lava flows.

Geologic setting

Karisimbi Volcano (1.50 S, 29.45 E) is part of the Virunga volcanic field, which forms a transverse chain in the western branch of the East African Rift (Fig. 1). At 4507 m it is the highest and one of the largest of the eight major volcanoes in the Virunga field (Fig. 2). Unlike Nyiragongo and Nyamuragira volcanoes farther west, Karisimbi is not active (although neighboring Visoke had a brief eruption in 1957).

Karisimbi volcanic rocks present an almost complete differentiation series of silica-undersaturated lavas,

Editorial responsibility: C. Newhall

Mary E. MacKay (✉) · Scott K. Rowland
Peter J. Mouginis-Mark · Harold Garbeil
Hawaii Institute of Geophysics and Planetology, University of Hawaii, 2525 Correa Road, Honolulu, HI 96822, USA
Fax: +808 956 6322
e-mail: mackay@soest.hawaii.edu

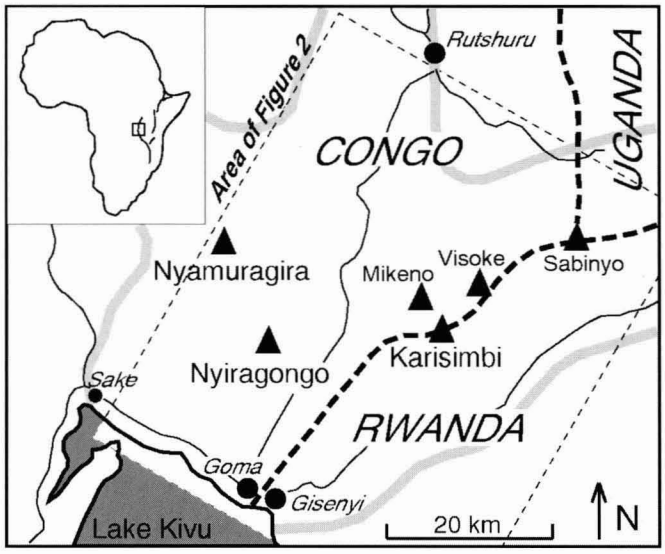

Fig. 1 Location map showing the main volcanoes of the Virunga volcanic field. *Dashed box* shows the location of Fig. 2. Approximate boundary of the Virunga volcanic field is marked by the *thick gray line*. *Bold dashed lines* mark political boundaries. *Inset* shows the area of Fig. 1 and the two major branches of the East African Rift zone

ranging from primitive K-basanites to evolved K-trachytes (DeMulder 1985). K-hawaiites are most abundant at the surface. They are overlain by the thick trachyte flows that are the focus of this paper (Figs. 3, 4). Seven samples from the trachyte flows yield a mean SiO_2 content of 61 wt.% (DeMulder 1985); K–Ar dating shows that the Karisimbi trachytes are younger than 0.010 Ma (DeMulder and Pasteels 1986).

Topographic mapping

Karisimbi and the eastern portion of the Virunga volcanic chain (excluding Nyiragongo and Nyamuragira) were imaged as part of the repeat-pass interferometry experiment during the October 1994 flight of the Spaceborne Imaging Radar-C (SIR-C; Stofan et al. 1995). Data were obtained on two consecutive days from nearly identical orbits (DT154.90 and DT170.90), with a calculated baseline separation of approximately 171 m and an incidence angle of ~26°. Radar interferometry exploits the very small angular difference in viewing geometry between two images to determine the phase difference (due to slightly different lengths of the two travel paths), from which we derive the DEM. The theory and application of radar interferometry are discussed in detail in Zebker and Goldstein (1986), Massonet and Rabaute (1993), Lin et al. (1994), and Zebker et al. (1994), and numerous references can be found on the NASA/JPL homepage at http://southport.jpl.nasa.gov/science/SARREFS.html. Although atmospheric effects can strongly influence the absolute elevation values in an interferometrically derived DEM (Rosen et al. 1996; Zebker et al. 1997), in this study we rely on the relative accuracy and noise level within the DEM.

Radar correlation is a measure of the similarity of the two radar images that make the interferogram. Within the boundaries of the forest preserve that encompasses Karisimbi's summit (Fig. 5), subtle changes in vegetation (due to wind, rain, or differences in viewing geometry) between the two observations causes noisy values in the DEM due to low correlation between the two scenes. Noisy areas produce dimpled regions in the shaded-relief image (Fig. 3), such as the low backscatter area just inside the southwest boundary of the forest preserve. Other than these few areas, relative height accuracy as a function of phase error (Zebker et al. 1994) is better than 10 m (as good as 2–3 m) in areas of strong correlation, which compose most of the scene. No DEM values exist where steep, radar-facing slopes exceed the geometric limits of the technique as a result of layover or foreshortening; these areas are black in Figs. 3, 4, and 6.

Because radar is unable to penetrate thick forest canopy, an interferometric DEM, such as that used here, may return elevations of the top or middle of the vegetation rather than the ground surface. Our flow-thickness calculations are based on relative heights, however, which remain accurate if the height of the vegetation is the same on the trachyte flows as on the surroundings. Several lines of evidence support this assumption. Firstly, the trachyte flows are approximately 10,000 years old and overlie a lava plain composed primarily of hawaiite flows which are $\leq$70,000 years old (DeMulder and Pasteels 1986). Both the trachyte flows and their surroundings are vegetated, and most areas outside the forest preserve are intensively farmed, even on steep slopes, producing shorter and more uniform vegetation than might naturally occur. Also, note that the height of the vegetation on the trachyte flows needs only to be similar to that of the surrounding lava plain (within the 2–3 m relative accuracy of the DEM, a small percentage of the 40–60 m flow thickness). Radar backscatter (Fig. 3), correlation (not shown), and Landsat Thematic Mapper data (not shown) are all sensitive to changes in vegetation. All of these data show the striking change in vegetation at the boundary between forest preserve and agricultural lands (Fig. 5); however, on either side of the boundary, lava flows and their surroundings appear to be similarly vegetated. In addition, those flows that cross the forest preserve boundary have the same apparent thickness on either side of the boundary, as expected if thickness estimates are little affected by vegetation. Finally, flow thickness calculated from the interferometric DEM agrees well with values obtained from the topographic map, for those flows that can be identified from the map (discussed below).

We created the DEM from the L-band (24 cm wavelength) SIR-C data, because correlation is much higher for the L-band than for the shorter wavelength C-band (5.6 cm) and the L-band is better suited to steep slopes.

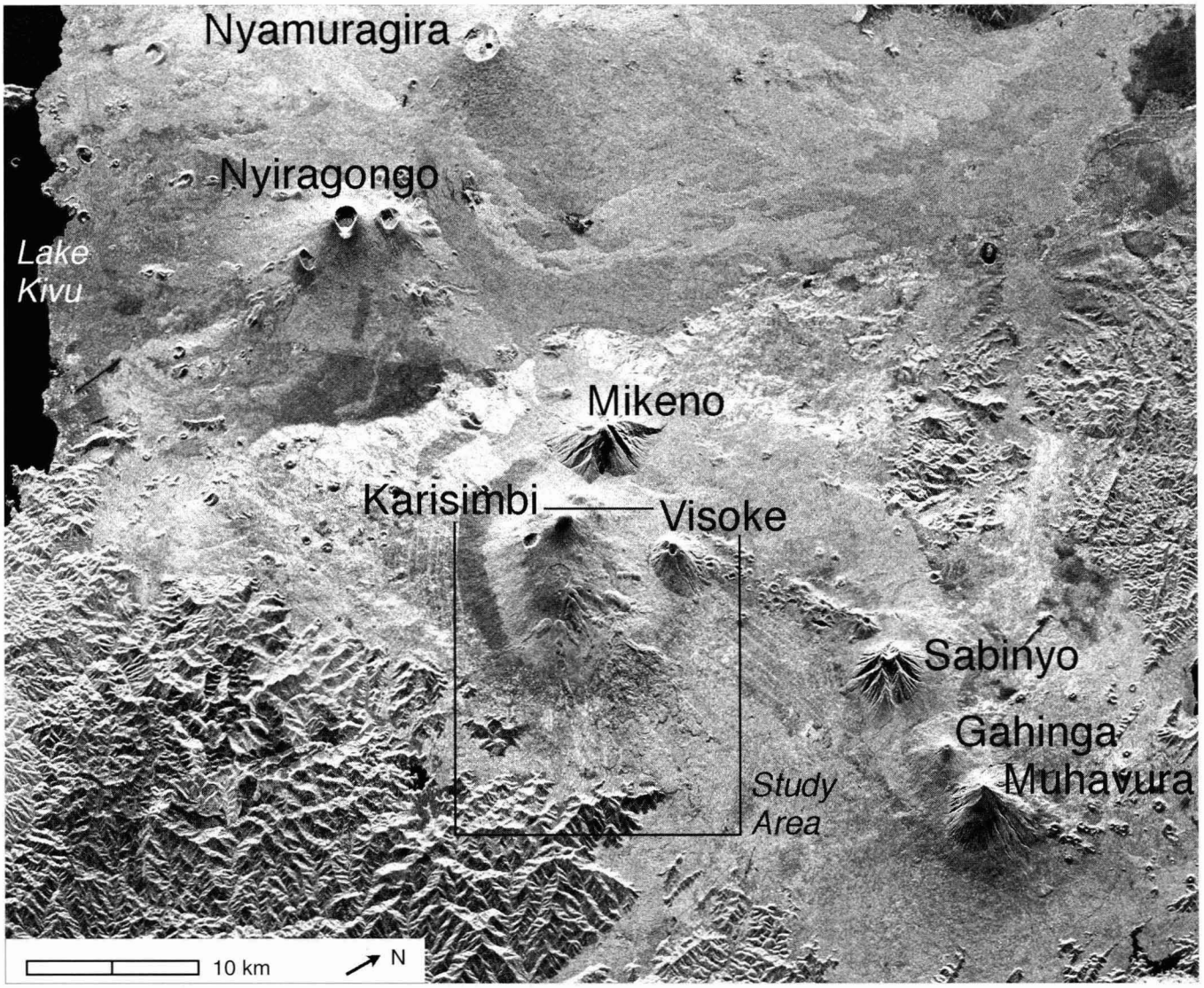

Fig. 2 SIR-C observation 171.1 showing the main volcanoes of the Virunga volcanic field and the location of the study area (SIR-C interferometric data do not cover Nyiragongo and Nyamuragira). Radar illumination is from the top (northwest) at an incidence angle of ~41°. This image is not corrected for topographic effects and shows "layover" of features at higher elevations, distorting the shape of the study area (and the scale in the vertical direction)

Longer wavelength data imply a less dense fringe spacing, which aids in phase unwrapping, the stage of processing in which relative phase is converted to absolute phase. The DEM and all subsequent processing was done at a 20.6-m pixel spacing. From the DEM we made a shaded-relief image for use in mapping (Fig. 3) and a flow thickness map (Fig. 6).

To generate the flow-thickness map, we first used the shaded-relief image to define the extent of flows and other positive relief features. We then took elevation values at every tenth pixel, excluding these defined positive relief features (Fig. 7). Using the Generic Mapping Tools (GMT; Wessel and Smith 1991), we fit an interpolated surface to these selected pixels. The resulting "no-flows" surface represents a smoothed version of the topography without the flows and other local topographic features. Subtracting the smoothed surface from the original DEM yields the flow-thickness map in Fig. 6.

Because the interpolated surface is very smooth, higher-frequency topographic features from the DEM show up as noise on the flow-thickness map. The most obvious (and easily ignored) examples of this are the peaks and valleys in the Precambrian mountain area (lower left corner of Fig. 6). Less obvious are the smaller variations spread across the area surrounding the flows. Excluding the trachyte flows and areas of high relief, such as the Precambrian mountains and Visoke Volcano, 93% of this background noise lies within ±10 m. The noise does not affect thickness or volume estimates (because the mean is near zero, positive and negative features will cancel), although subtle features beneath this threshold cannot be distinguished from the

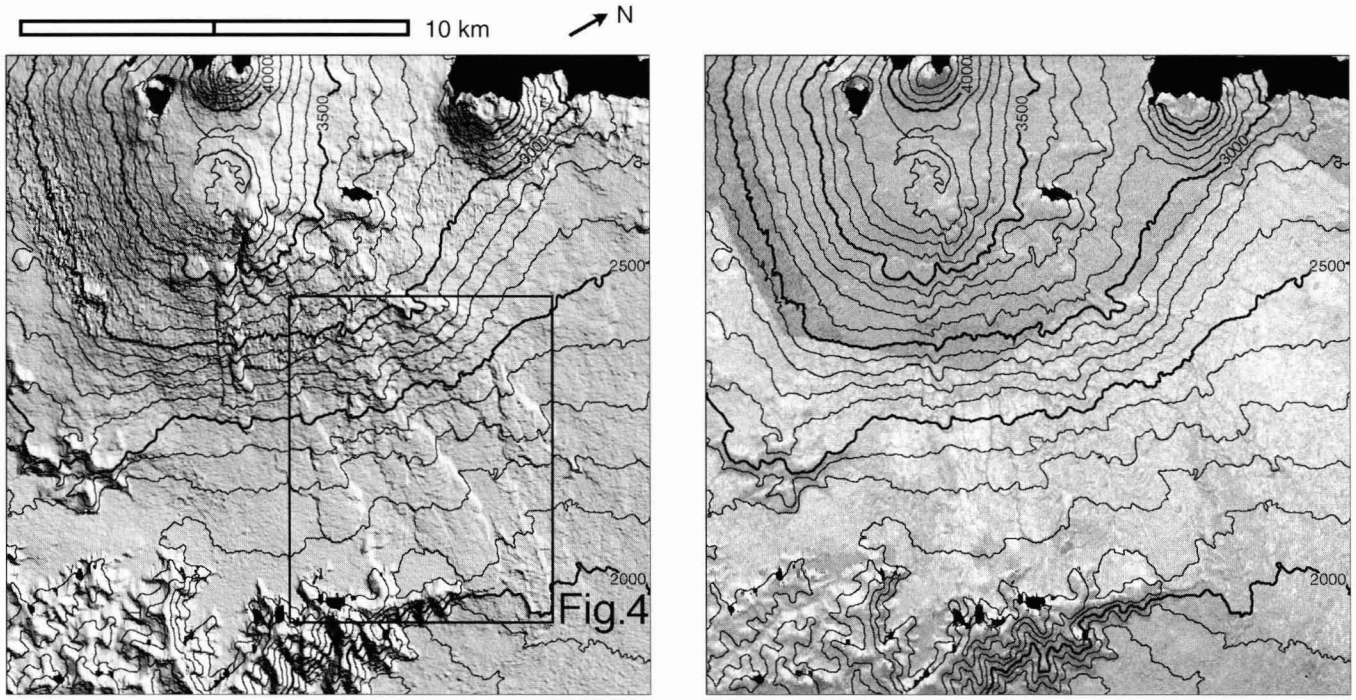

Fig. 3 Shaded-relief digital elevation model (DEM) and radar backscatter (L-band, vertically polarized), overlain with 100-m contour lines. *Box* shows the location of Fig. 4. Shaded-relief image is illuminated from the upper-right corner to enhance flow boundaries; backscatter is illuminated from the top of the image. Dark, low backscatter region at higher elevations of Karisimbi and Visoke reflects different vegetation within the forest preserve (boundary shown in Fig. 5)

background noise. For the trachyte flows, the thickness shown is a minimum value, because flows may have occupied topographic lows that cannot be estimated by this method.

In Fig. 8 we compare the DEM and "no-flows" surface to values from the previously published topographic contour map (Thonnard et al. 1965) along four profiles. This comparison provides both an independent test of the relative accuracy of the DEM and highlights the difference in topographic detail between the DEM and the contour map. On all four profiles, flow thicknesses are similar in the DEM and contour map, although two of the profiles (flows 11 and 10) show lower absolute elevations on the contour map. In plan view (not shown), flow 3 appears wider, and flow 11 narrower, on the contour map than in the shaded relief. Only the extreme distal portion of flow 12 (which is thicker than the rest of the flow) can be seen in the contour map; flows 5 and 6 are not evident in the contour map, nor are the upper reaches of most flows. The areal extent of the flows is confirmed by comparing the flow margins seen in the shaded-relief image with those observed in the radar backscatter image (Fig. 3). Although the DEM (and derived shaded-relief image) might be subject to height error that could create false

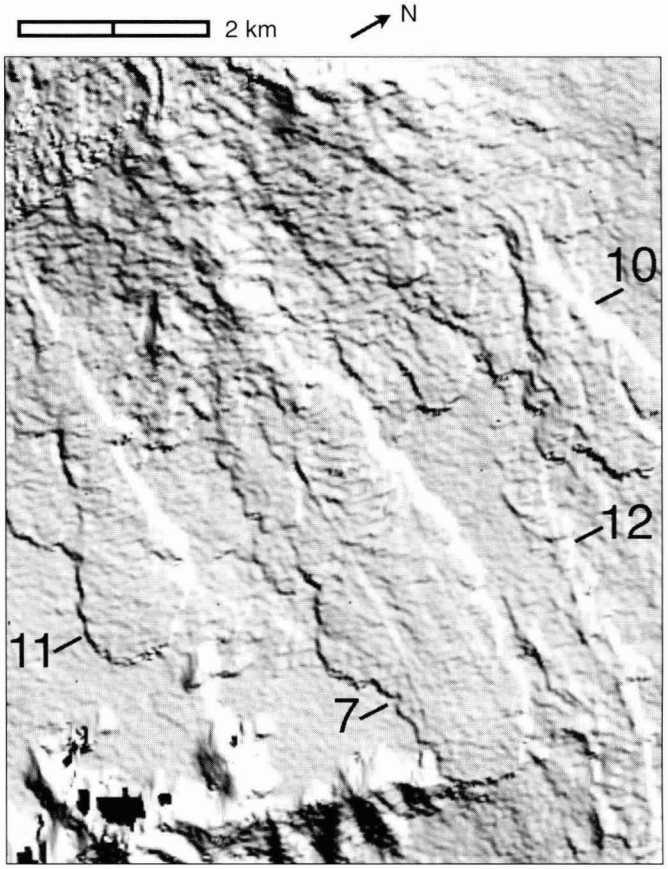

Fig. 4 Enlargement of shaded-relief DEM showing the distal portion of several flows; location shown in Figs. 3 and 5. Note the prominent shear zones and arcuate ridges on flow 7 and well-developed channels on flows 7 and 10

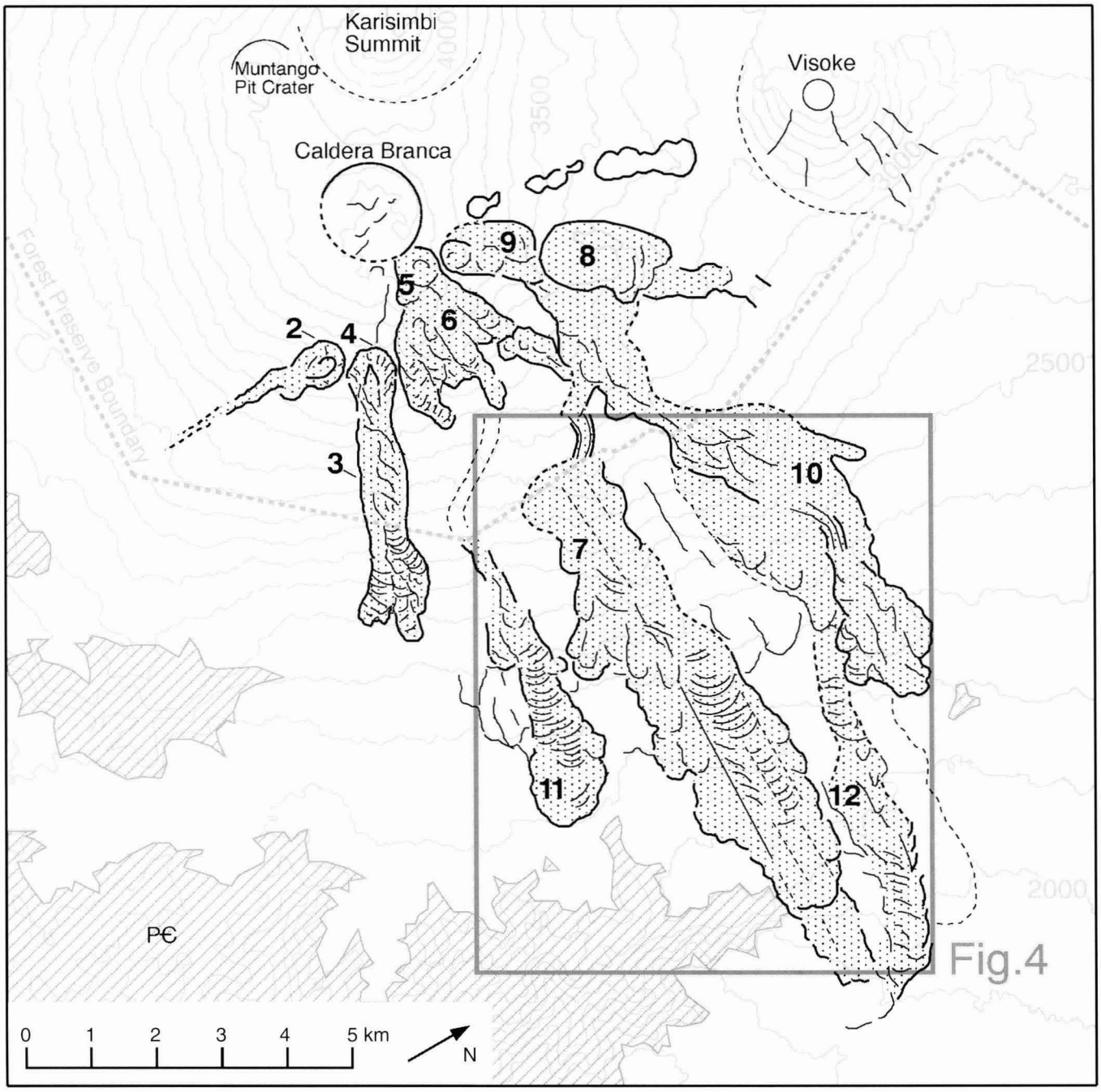

Fig. 5 Map of flow morphology showing major flows (*stippled*) and flow structures seen in shaded-relief, backscatter, and flow thickness images. *Box* shows the location of Fig. 4. *Thicker line* weights are more prominent features, *dashed lines* are indistinct boundaries. *Hatched area* is mountainous Precambrian basement. There is no flow 1

flow margins, the margins seen in the radar backscatter result from illumination and shadow of the Earth's surface and are not subject to the same sort of potential error.

Although most of our mapping is done from shaded-relief images, the flow-thickness map is also useful for mapping flows where flow boundaries are indistinct and poorly expressed in the radar backscatter and shaded-relief images. Shaded-relief images (with various illumination directions) tend to highlight those features whose boundaries have significant relief (to catch the "light" or cast shadow); the same is true of radar backscatter in cases such as ours, where large areas have similar backscatter values. Features with subtle or gradational topographic boundaries do not stand out in such images. For example, the inferred proximal section of flow 11 (dashed line in Fig. 5) cannot be traced in any of our shaded-relief images. Although not obvious, the thickness map shows a likely path for this

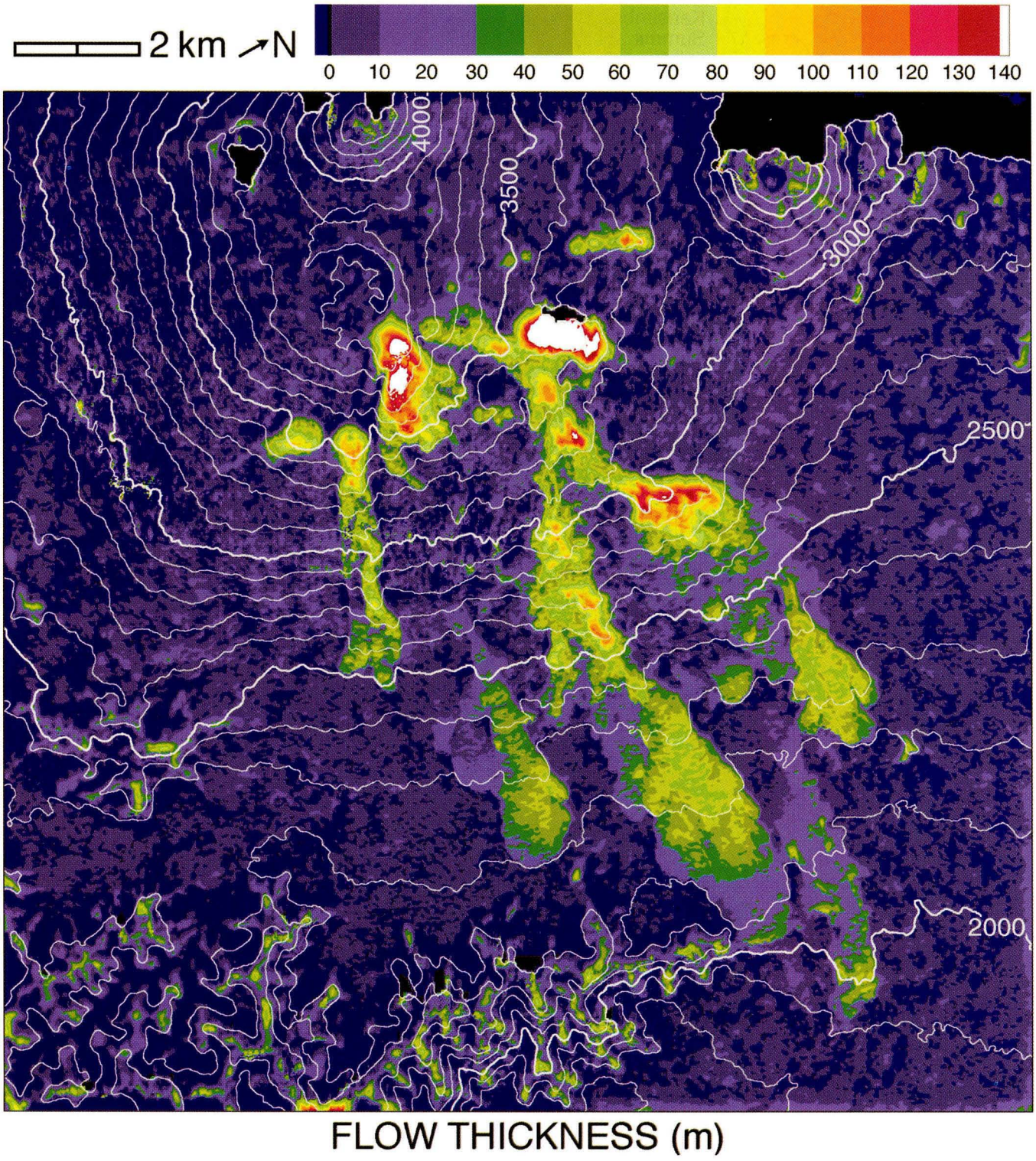

Fig. 6 Flow thickness (in meters), overlain with 100-m contour lines. Thickness was estimated by subtracting an interpolated reference surface from the DEM. Scattered highs in the Precambrian mountains are topographic artifacts. Background noise is ±10 m. Flow dimensions and volumes are given in Table 1

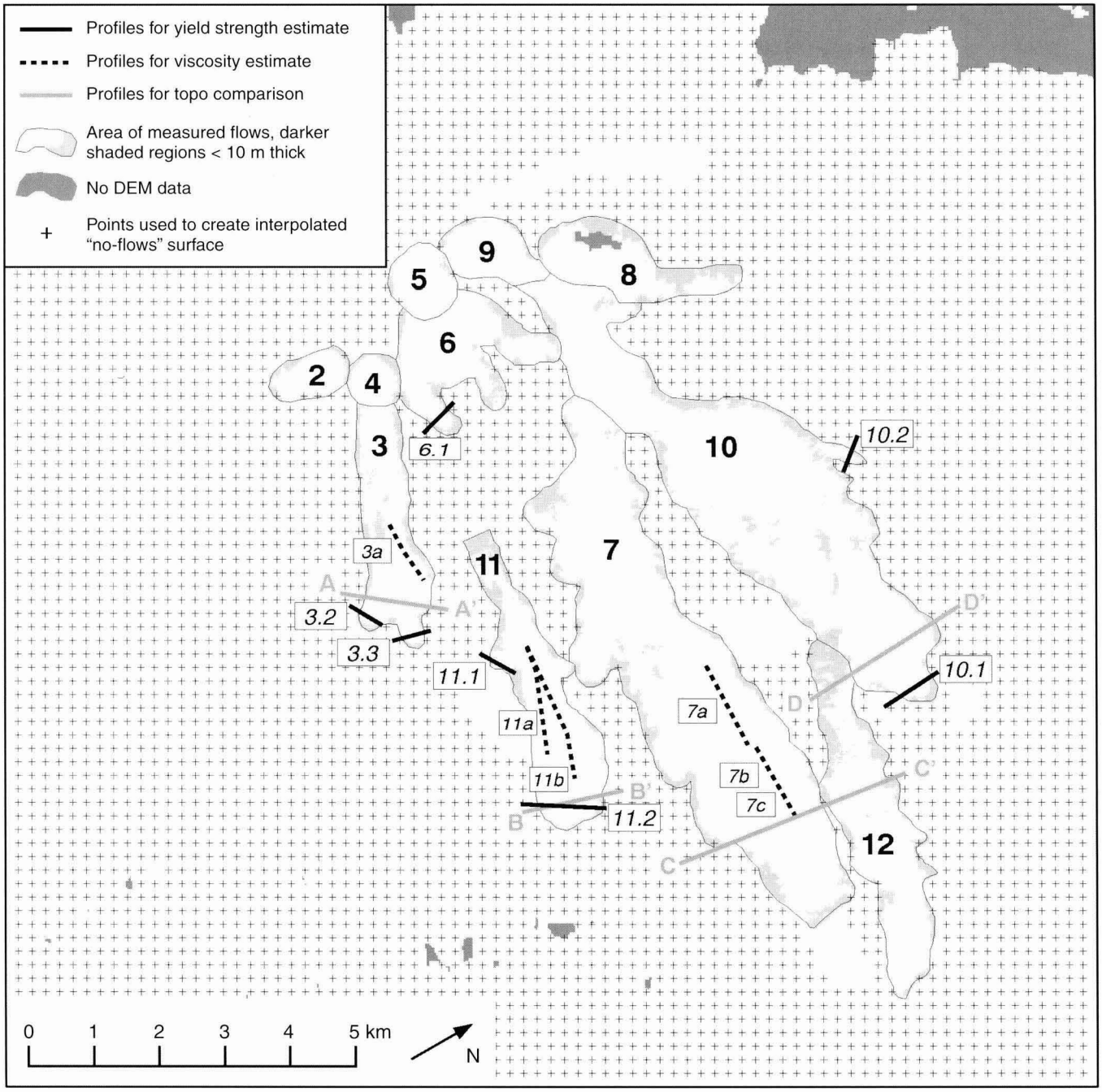

Fig. 7 Numbered flow units, showing location of profiles used for yield strength (*black lines*) given in Table 2, apparent viscosity (*dashed lines*) given in Table 3, and profiles compared with topographic map in Fig. 8 (*gray lines*). Only *light-gray* areas were used in area/volume calculations; *medium gray areas* at edges of flows have thickness <10 m and were not included. *Dark gray areas* (black in Figs. 3 and 6) are data gaps produced by steep radar-facing slopes. *Crosses* show points used in interpolation of the "no-flows" surface, which omits flows and other local topography

flow (Fig. 6), which may have originated as a breakout from flow 6.

Flow dimensions

We use flow thicknesses shown in Fig. 6 to calculate volumes of the most prominent flows and domes. Within the flow boundaries (Fig. 7), we include only those pixels with a thickness ≥10 m (the level of background topographic noise in the thickness image) in the calculations, thereby producing conservative estimates of area and volume as shown in Table 1. The largest of the

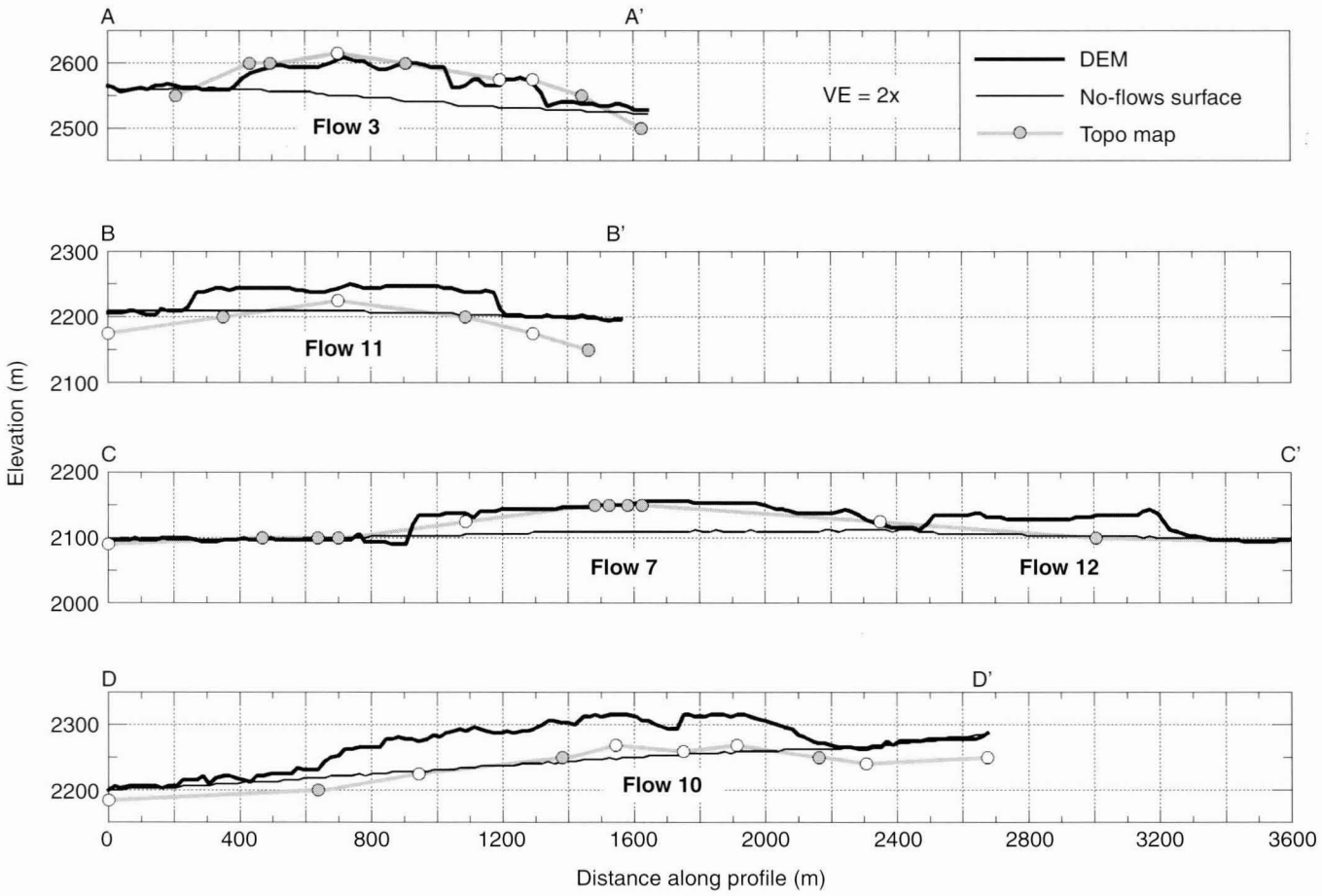

Fig. 8 Profiles comparing DEM and contour values from the topographic map (Thonnard et al. 1965). Profile locations are shown on Fig. 6. *Closed circles* are contour crossings, and *open circles* are interpolated from the topographic map. The "no-flows" surface was subtracted from DEM values to get the flow thickness shown in Fig. 6. Vertical exaggeration (VE) is 2×

Table 1

Flow Number	Flow Dimensions				Notes
	Length (km)	Area (km^2)	Volume (km^3)	Mean Height (m)	
2		0.6	0.03	49	dome
3	3.8	2.3	0.10	43	single flow
4		0.4	0.03	62	dome
5		0.9	0.08	94	dome
6	2.2	2.3	0.13	56	coulée
7	8.9*	11.9	0.50	42	branch flow
8		1.5	0.14	90	domes
9		1.1	0.05	43	domes
10	10.1	11.0	0.51	47	branch flow
11	7.6	3.1	0.11	35	single flow
12	4.5	3.3	0.09	27	older flow
7+10		22.9	1.01	44	two-branch
ALL		38.5	1.77	46	all flows

* Length of branch from flow 10; total length from vent = 11.9 cm

flows is almost 12 km long, covers an area of 23 km^2, and has a volume of more than 1 km^3 distributed in two major branches (flows 7 and 10; Fig. 7). Because of the inherent ambiguity in interpreting temporal relationships between flows from remote sensing data, we have treated calculations for flow 7 and flow 10 separately. Although flow 7 appears to be a major branch originating as a breakout from flow 10 approximately 2 km from the vent, it is also possible that flow 7 predates flow 10. The combined flows 7 and 10 account for almost two thirds of the total volume of trachyte calculated in this study. Flows 3 and 11 are similar to each other in volume ($\sim$0.1 km^3); however, because we are unable to confidently trace flow 11 to the vent, its area and volume are certainly larger than shown. Features 2, 4, 5, 8, and 9 are lava domes rather than lava flows, and flow 6 is an extremely thick flow that may be more appropriately termed a coulée. It is clear from the shaded-relief image, and comparison with flow maps in DeMulder (1985) and Marcelot et al. (1985), that numerous flows with less clearly defined boundaries and topographic expression are present but are not included in our calculations. We calculate a total volume of almost 1.8 km^3 for all of the mapped flows, still far short of DeMulder's estimate of $\sim$3 km^3 for the thick trachyte flows of Karisimbi's east flank.

Flow structures

The shaded-relief image is particularly valuable for basic mapping. We have been unable to find air photographs, optical satellite images (e.g., SPOT data) are not available for Karisimbi, and the radar backscatter images are not very helpful because of the low incidence angle and heavy vegetation. We created a series of shaded-relief images using different illumination azimuths to highlight and map a variety of features. Features oriented nearly perpendicular to the illumination direction are enhanced and those approximately parallel are subdued; therefore, multiple shaded-relief images are necessary to map features of different orientations. Only one of these images is shown here (with illumination from the north), although all were used in the interpretation shown in Fig. 5. Numerous flow structures, such as overlapping flow units, channels, and arcuate ridges, can be seen in the shaded-relief image (Fig. 3). Based on their shape and widespread occurrence, we interpret the arcuate ridges to be folds formed in the viscous crust as the lava flow backed up behind the slowing toe of the flow. One of the best examples of these features is the distal portion of flow 7, where distinct shear zones separate levees from a central region marked by large arcuate ridges (Fig. 4). In the region of profile 7a (Fig. 7), the folds extend across the surface of the entire channel for approximately 1.5 km along the length of the flow. Downslope, the flow becomes more complex and develops two adjacent channels. The northern ends of the folds in the southern channel are bent downflow, indicating a velocity contrast between the north and south channels (Figs. 4, 5). This may have occurred as the southern half of the flow encountered the Precambrian mountains, whereas the northern half of the flow was able to overrun the much lower northern end of the range.

Rheological properties of flows

Numerous relationships have been developed for estimating rheological parameters by measuring the dimensions of stationary lava flows (e.g., Hulme 1974); these have been used mostly in extraterrestrial settings where only image data are available. Although the assumptions underlying these estimates greatly oversimplify the behavior of lava flows, they are often the only source of rheological information available. There are no field measurements of rheology for viscous flows such as those found on Karisimbi. Given the rarity of eruptions that produce these types of flows and the difficulty one would encounter attempting to make such measurements on an active, 40-m-thick lava flow, we include estimates of yield strength and apparent viscosity for comparison with previous estimates derived for thick flows elsewhere (e.g., Friedman et al. 1963; Hulme 1974; Moore et al. 1978; Fink 1980; McBirney and Murase 1984; Zimbelman 1985; Wadge and Lopes 1991; Pinkerton and Stevens 1992). The usefulness of such estimates lies more in stimulating our thinking about the factors that interact to influence flow behavior and morphology (such as slope, effusion rate, cooling, and rheology) than in the numbers themselves.

Yield strength estimate

Yield strength estimates are based on the assumption that lava flows can be approximated as Bingham fluids and that they will spread laterally or downslope until the combination of gravity, flow density, flow thickness, and slope can no longer overcome the yield strength of the flow. We selected profiles across individual flow lobes and calculated yield strength from the height, width, and slope of the flow using two different equations:

	Width method	Slope method
Yield strength (S_y):	$S_{yw}=\rho g h^2/w$	$S_{y\theta}=\rho g \sin(\theta) h$

in which ρ=bulk density (2000 kg/m^3), g=gravity (9.8 m/s^2), h=height of flow, w=width of flow, and θ=slope of the underlying surface (Hulme 1974; Moore et al. 1978). Width is easily determined in the DEM from the sharp inflection points (often local minima) at the base of the flow profile. Because the upper surface of each flow is so irregular, we used the mean value of

Table 2

Flow Number	Profile Number	Flow Dimensions				Yield Strength (kPa)*			Notes
		Base Slope (deg)	Flow Width (m)	Flow Height (m)	Aspect Ratio	S_{yw}, Width Method	$S_{y\theta}$, Slope Method	Ratio $S_{y\theta}/S_{yw}$	
3	3.2	9.1	332	32	0.10	61	100	1.6	
3	3.3	7.7	300	35	0.12	80	92	1.1	
6	6.1	14.5	247	40	0.16	124	194	1.6	
10	10.1	4.2	668	41	0.06	49	59	1.2	
10	10.2	9.2	195	25	0.13	64	80	1.2	side lobe
11	11.1	7.3	378	30	0.08	48	75	1.6	side lobe
11	11.2	2.8	909	33	0.04	24	31	1.3	main lobe

* Measurement errors may produce errors in yield strength as high as 60% of value

height above those minima (for all points within 20 m elevation of the maximum height) for flow height. Underlying topographic slope is taken from the interpolated "no-flows" surface at the midpoint of the particular flow profile. Following Wadge and Lopes (1991) we attempted to select profiles that cross a simple terminal lobe (locations shown in Fig. 7), assuming that the morphology of the terminal lobes should most closely represent the yield strength of the lava. Table 2 lists the calculated values for yield strength, which range from 23 to 124 kPa for S_{yw}, comparable to similar yield-strength estimates for Hawaiian trachyte flows (23–110 kPa; Moore et al. 1978). If we assume measurement errors of 1 pixel for width (20.6 m), 10 m for height (the level of background noise), and 2° for slope, possible measurement errors for yield strength are of the order of 60% for both width and slope methods. Variation in yield strength is correlated with underlying slope; lower values of yield strength correspond to lower basal slopes for both methods, as noted by Moore et al. (1978) for a variety of flows. This apparent correlation may result from the failure of either of the simple models to completely account for the influence of slope on morphology and the resulting yield-strength estimate. We note, however, that those flows with lower calculated yield strength had to flow the farthest just to reach the lower slopes at the base of Karisimbi. The yield-strength estimates may therefore reflect true differences in the rheology of the lavas, perhaps due to differences in eruptive parameters such as effusion rate, volume, or temperature. Where we have two values for a single flow (flows 3, 10, and 11) the yield strength estimates differ by approximately 20 kPa, with the side lobe estimates of flows 10 and 11 producing higher values than those of the associated main flow. As one would expect from its morphology, the yield-strength estimate for flow 6, emanating from the dome just upslope, is the highest of our calculated values at 124 kPa. $S_{y\theta}$ is also calculated for comparison with S_{yw}. For most of the profiles, the two methods produce similar results with $S_{y\theta} > S_{yw}$; however, profiles 3.2, 6.1, and 11.1 give $S_{y\theta}$ values approximately 1.6 times that of S_{yw} and provide a second estimate of possible error. Similarly, Moore et al. (1978) reported $S_{y\theta}$ values typically twice those of S_{yw}.

Apparent viscosity estimate

The dimensions and behavior of these flows are very different from familiar basalt and andesitic flows. An average Karisimbi trachyte flow is 40–60 m thick. The upper slopes of Karisimbi (within 4–5 km of the vent) average 10–15°; lower elevation slopes are 3–8° for those flows that reach them. Applying the Jeffreys equation ($V_{\text{elocity}} = (\rho g\, h^2 \sin\theta)/(3\,\eta)$, where η = viscosity), a 40-m-thick flow with a viscosity of 10^9–10^{11} Pa s can achieve a velocity of 3 m/h to 0.03 m/h on a 5° slope, and twice that value on a 10° slope. At these speeds it could take from 32 days to 9 years to travel 5 km on a 10° slope. Manley (1992) argues that large rhyolite flows cool so slowly that they may remain active for decades; however, it is hard to imagine that these lava flows were emplaced at viscosities much higher than 10^{11} Pa s, as emplacement time increases proportional to the viscosity.

We used the technique of Fink (1980) to estimate surface and interior viscosities from the height and spacing of the folds on flows 3, 7, and 11, using the following relations (Fink and Fletcher 1978):

$$\eta_0 > (\rho g t_c)/(0.08 \ln \mathrm{R}\, E_{xx}) \quad R = \eta_0/\eta_i \quad \ln R > 28 t_c/d$$

where t_c = thickness of the folding crust (in some cases approximated by ridge height), d = arc length of the folds, R = ratio of the surface viscosity (η_0) to interior viscosity (η_i), and E_{xx} = compressive strain rate. This technique relates the height and spacing of surface folds to the apparent viscosity of a flow and requires an estimate of the thickness of the crust and the time interval over which the folds formed. Because we have few constraints on the thickness of the folding crust and none on the duration of the folding event, we have calculated viscosity using a range of values for these two parameters. Variation in thickness of the crust affects only the interior viscosity values, whereas the duration of folding (and therefore E_{xx}) affects both surface and interior viscosity estimates. In addition, we have some limits on crustal thickness (0–100% of flow), whereas strain rate is only scantily constrained by common sense.

Because this method assumes Newtonian behavior, but these flows are clearly non-Newtonian (i.e., they have yield strengths), calculated viscosities are actually apparent viscosities for a given strain rate. The lower the strain rate (the longer the duration of folding or the smaller the estimated strain), the greater the apparent viscosity. This dependence (and lack of constraint) on strain rate introduces such large uncertainties in the viscosity calculations that the numbers may only have qualitative usefulness. This is true for most estimates of viscosity, whether from laboratory or field data. Pinkerton and Stevens (1992) and McBirney and Murase (1984) give excellent summaries of some of the problems associated with viscosity estimates; thus, this analysis is useful in comparing rheology of these flows with each other and with other morphology-based estimates, such as those of Friedman et al. (1963), Fink (1980), and Zimbelman (1985), but we warn against using the resulting values in any quantitative application.

We measured fold dimensions from the DEM (Table 3) and calculated apparent viscosity using folding-crust thickness of 10, 20, and 30% of total flow thickness. Note that a thin crust, such as 10% of total flow thickness, results in very low calculated viscosity contrast (low R; Table 3) and is thus less likely to fold. Shortening was computed by comparing the surface length of the profile (original length) to the straight line distance between the two endpoints (folded length).

Because we are working at the spatial resolution of the SIR-C data and therefore cannot resolve features smaller than 20 m, we used twice the measured shortening for the estimated strain; true strain may be many times this value. Fink (1980) and Zimbelman (1985) use 50% strain in their calculations, resulting in viscosities an order of magnitude lower than ours. Viscosities in Table 3 are computed using one day as the duration of folding, but days or weeks are possible given the probable slow velocity of the flows. Assuming a strain interval of 24 h and 20% total thickness as the thickness of the folding surface, we obtain apparent viscosity values ranging from 7.5×10^{10} to 5.2×10^{11} Pa s for the interior viscosity of the flows, and 1.2×10^{12} to 5.5×10^{12} Pa s for the surface viscosity. Although these values are poorly constrained as discussed above, they seem to be in relative agreement with field relationships of these flows and viscosity estimates for other viscous flows. For example, the apparent viscosity of flow 7 increases downflow, and flow 7 values are higher than those of the shorter flows 3 and 11. This is consistent with the observation of Fink and Zimbelman (1986) that viscosity increases downflow for recent basalt flows on Kilauea Volcano, Hawaii. Surface viscosities are similar to those obtained by Fink (1980) for the Glass Mountain rhyolite and Chao dacite flows for the same time interval, but we calculate much higher interior viscosities (and thus lower viscosity ratios) due to the longer fold arc length to height ratio at Karisimbi and low estimated strain used in our analysis. A trachyte flow on Hualalai Volcano, Hawaii, has ridges of similar dimension [15 m height, 150 m spacing; Macdonald and Abbott (1970)] to those found on Karisimbi, and has an estimated apparent viscosity of 1.7×10^{11} Pa s for a strain interval of 1 day (using 50% strain; Zimbelman 1985). Other techniques yield a range of viscosity values. For example, Friedman et al. (1963) use the Jeffreys equation and limited observations of flow geometry and velocity to estimate an apparent viscosity of 10^9–10^{10} Pa s for the 1953 Trident dacite eruption. Laboratory and theoretical estimates of viscosity, such as those of Pinkerton and Stevens (1992) and McBirney and Murase (1984), report viscosities of 10^9–10^{12} Pa s for the Mount St. Helens dacite.

With viscosity estimates ranging over three orders of magnitude, there remains much to be understood about the behavior of viscous lava flows. In our case, the morphologic features on which both yield-strength and viscosity analyses are based tend to be located in the distal portions of the flows. Both yield strength and viscosity are estimated some distance from the vent, resulting in values that are higher than the initial conditions, particularly for viscosity. In addition, the apparent viscosity of a non-Newtonian lava may be higher at low velocities than at high velocities if the ratio of strain rate to shear stress is not linear (McBirney and Murase 1984). It is also important to keep in mind that estimates of this type are for bulk properties of the flow, including not only melt, but solids and gases. A more viscous

Table 3

Profile Number	Fold Dimensions						Ratio of Surface/Interior Viscosity			Exx (24 hr) Strain Rate (s^{-1})	Apparent Viscosity (24 h) (Pa s)			
	Fold Height (m)	Fold Spacing (m)	Estimated Strain	Arclength d (m)	Flow Height h (m)	20% h t_c (m)	20% h d/t_c	10% h R	20% h R	30% h R		Surface Viscosity	10% h Interior	20% h Interior	30% h Interior
7a	13	124	5.2%	130.9	60.3	12.1	10.9	3.6	13.2	47.9	6.0E−07	1.9E+12	5.2E+11	1.4E+11	4.0E+10
7b	6	93	3.4%	96.2	53.0	10.6	9.1	4.7	21.9	102.5	4.0E−07	2.1E+12	4.6E+11	9.7E+10	2.1E+10
7c	7	124	1.7%	126.1	53.0	10.6	11.9	3.2	10.5	34.1	2.0E−07	5.5E+12	1.7E+12	5.2E+11	1.6E+11
11a&b	8	96	5.3%	101.3	42.1	8.4	12.0	3.2	10.2	32.8	6.1E−07	1.5E+12	4.6E+11	1.4E+11	4.4E+10
3a	14	111	7.2%	118.7	59.6	11.9	10.0	4.1	16.6	67.8	8.4E−07	1.2E+12	3.0E+11	7.5E+10	1.8E+10
Glass Mt*	16	39	23%	48		10	4.8		1E+04		1.1E−08	2.4E+13		2.4E+09	
Chao*	30	200	20%	240		30	8		33.1		5.8E−06	3.6E−11		1.1E+10	

* Values from Fink (1980).
Crustal thickness values are given for t_c (thickness of folding crust) = 10%, 20%, or 30% of flow thickness, h. Exx, compressive strain rate. Strain rate and viscosity are given for a folding interval of 24 hours; for other intervals divide strain rate, or multiply viscosity, by the number of days. Because of the unconstrained dependence on strain rate, errors for viscosity estimates are several orders of magnitude

crust, indicated by the formation of surface folds, may play a key role in the behavior and final morphology of the flow (Blake 1990; Griffiths and Fink 1993), thereby influencing the results for yield strength and other morphologic analyses. As Griffiths and Fink (1993) note, for most flows lava rheology is heterogeneous and cannot be characterized by a single yield strength or viscosity.

Conclusions

For poorly mapped flows such as those at Karisimbi, the gathering of basic mapping and morphologic data adds another set of flows for comparison to the limited number of viscous flows that have been studied. These rheological estimates are useful for thinking about the behavior of thick flows but must be understood to have large uncertainties. Nevertheless, they raise interesting questions about the relationship between yield strength, slope, and the distance flows have traveled from the vent (low yield-strength flows have traveled farthest) and about how these flows developed structures (channels, levees, shear zones, surface folds) similar to those of flows many orders of magnitude less viscous.

The growing availability of DEMs from radar interferometry will allow the study of the morphology of inaccessible or cloud-covered volcanoes in unprecedented scale and detail (compared with standard topographic maps or their derived DEMs). Basic mapping from shaded-relief and backscatter images, coupled with techniques such as slope analysis (Rowland 1996; Mouginis-Mark et al. 1996) and flow thickness estimation, can provide much-needed estimates for the extent and emplacement of lava flows as well as other volcanic features. If these morphologic data are combined with field observations, reasonable estimates of yield strength and viscosity can be made, in some cases allowing estimates of effusion rate (de Silva et al. 1994) and other eruptive parameters. Equally exciting are the possibilities for comparative and planetary volcanology (Theilig and Greeley 1986) that will arise when high-quality DEMs become more widely available from instruments such as the Mars Orbiter Laser Altimeter. Just as volcano morphology holds clues to the evolution of individual volcanoes, comparative morphology holds the promise of new insights into lava flow behavior, vent locations, and the interaction of tectonic and volcanic events through detailed mapping of areas such as Nyiragongo, Erta Ale, and other rift zone volcanoes. The upcoming Shuttle Radar Topography Mission (SRTM), due to be launched in the year 2000, will collect the necessary data for DEMs at 30 m resolution with worldwide coverage at latitudes less than 60°. For volcanology this means the opportunity to map heretofore rarely seen volcanoes and to expand both scientific knowledge and hazard analysis on a global scale.

Acknowledgement This paper was improved by critical reviews from T. Gregg and an anonymous reviewer, and encouraged by kind words from various readers; we deeply appreciate both. This work was supported by JPL contract no. 958457 from the SIR-C/X-SAR program. This is Hawaii Institute of Geophysics and Planetology paper no. 1012 and SOEST contribution no. 4678.

References

Blake S (1990) Viscoplastic models of lava domes. In: Fink JH (ed) IAVCEI Proc Volcanology, vol 2. Lava flows and domes: emplacement mechanisms and hazard implications. Springer, Berlin Heidelberg New York, pp 88–126

DeMulder M (1981) Contribution a l'etude geomorphologique du volcan Karisimbi, Chaine des Virunga, (Republique du Rwanda). Rapport Annuel – Musee Royal de l'Afrique Centrale. Departement dc Geologie et dc Mineralogie, 1980, pp 97–109

DeMulder M (1985) The Karisimbi Volcano (Virunga). Annalen – Koninklijk Museum voor Midden-Afrika. Reeks in 8 (super 0) Geologische Wetenschappen –Annales – Musee Royal de l'Afrique Centrale. Serie in 8 (super 0). Sciences Geologiques, p. 90

DeMulder M, Pasteels P (1986) K–Ar geochronology of the Karisimbi Volcano (Virunga, Rwanda–Zaire). J Afr Earth Sci 5 (6): 575–579

Fink J (1980) Surface folding and viscosity of rhyolite flows. Geology 8 (5): 250–254

Fink JH, Fletcher RC (1978) Ropy pahoehoe: surface folding of a viscous fluid. J Volcanol Geotherm Res 4:151–170

Fink J, Zimbelman JR (1986) Rheology of the 1983 Royal Gardens basalt flows, Kilauea Volcano, Hawaii. Bull Volcanol 48:87–96

Friedman I, Long W, Smith RL (1963) Viscosity and water content of rhyolite glass. J Geophys Res 68:6523–6535

Griffiths R, Fink J (1993) Effects of surface cooling on the spreading of lava flows and domes. J Fluid Mech 252:667–702

Hulme G (1974) The interpretation of lava flow morphology. Geophys J R Astron Soc 39:361–383

Lin Q, Vesecky JF, Zebker HA (1994) Comparison of elevation derived from INSAR data with DEM over large relief terrain. Int J Remote Sensing 15:1775–1790

Macdonald GA, Abbott AT (1970) Volcanoes in the sea. University of Hawaii Press, Honolulu

Manley CR (1992) Extended cooling and viscous flow of large, hot rhyolite lavas: implications of numerical modeling results. J Volcanol Geotherm Res 53:27–46

Marcelot G, Rancon JP, Demange J (1985) The potassic series of Karisimbi Volcano (Virunga Range, Rwanda); volcanological and petrological aspects. J Volcanol Geotherm Res 26 (1–2): 99–129

Massonet D, Rabaute T (1993) Radar interferometry: limits and potential. IEEE Trans Geosci Remote Sensing 31:455–464

McBirney AR, Murase T (1984) Rheological properties of magmas. Ann Rev Earth Planet Sci 12:337–357

Moore HJ, Arthur DWG, Schaber GG (1978) Yield strength of flows on the Earth, Mars, and Moon. Proc Lunar Planet Sci Conf 9:3351–3378

Mouginis-Mark PJ, Rowland SK, Garbeil H (1996) Slopes of western Galapagos volcanoes from airborne interferometric radar. Geophys Res Lett 23:3767–3770

Pinkerton H, Stevens RJ (1992) Methods of determining the rheological properties of magmas at sub-liquidus temperatures. J Volcanol Geotherm Res 53:47–66

Rosen PA, Hensley S, Zebker HA, Webb FH, Fielding EJ (1996) Surface deformation and coherence measurements of Kilauea Volcano, Hawaii, from SIR-C radar interferometry. J Geophys Res 101:23109–23125

Rowland SK (1996) Slopes, lava flow volumes, and vent distributions on Volcan Fernandina, Galapagos Islands. J Geophys Res 101 (27): 657–672

Silva SL de, Self S, Francis PW, Drake RE, Ramirez CR (1994) Effusive silicic volcanism in the central Andes: The Chao dacite and other young lavas of the Altiplano-Puna volcanic complex. J Geophys Res 99:17805–17825

Stofan ER, Evans DL, Schmullius C, Holt B, Plaut JJ, van Zyl J, Wall SD, Way J (1995) Overview of results of spaceborne imaging radar-C, X-band Synthetic Aperture Radar (SIR-C/X-SAR). IEEE Trans Geosci Remote Sensing 33:817–828

Theilig E, Greeley R (1986) Lava flows on Mars: analysis of small surface features and comparisons with terrestrial analogs. J Geophys Res 91:E193–E206

Thonnard RLG, Denaeyer NE, Antun P (1965) Carte Volcanologique des Virunga, Afrique Centrale, Feuiile no. 1, 1:50,000, Centre National de Volcanologie, Belgium

Wadge G, Lopes, RMC (1991) The lobes of lava flows on Earth and Olympus Mons, Mars. Bull Volcanol 54:10–24

Wessel P, Smith WHF (1991) Free software helps map and display data. EOS Trans AGU 72:441

Zebker HA, Goldstein R (1986) Topographic mapping from interferometric SAR observations. J Geophys Res 91: 4993–4999

Zebker HA, Rosen P, Hensley S (1997) Atmospheric effects in interferometric synthetic aperture radar surface deformation and topographic maps. J Geophys Res 102:7547–7563

Zebker HA, Werner CL, Rosen PA, Hensley S (1994) Accuracy of topographic maps derived from ERS-1 interferometric radar. IEEE Trans Geosci Remote Sensing 32:823–836

Zimbelman JR (1985) Estimates of rheological properties for flows on the Martian volcano Ascraeus Mons. J Geophys Res 90:D157–D162